STRUCTURAL BIOLOGY

Structures of ribosome-bound initiation factor 2 reveal the mechanism of subunit association

2016 © The Authors, some rights reserved; exclusive licensee American Association for the Advancement of Science. Distributed under a Creative Commons Attribution NonCommercial License 4.0 (CC BY-NC).
10.1126/sciadv.1501502

Thiemo Sprink,[1] David J. F. Ramrath,[1] Hiroshi Yamamoto,[1] Kaori Yamamoto,[1] Justus Loerke,[1] Jochen Ismer,[1]* Peter W. Hildebrand,[1]* Patrick Scheerer,[1†] Jörg Bürger,[1,2] Thorsten Mielke,[1,2] Christian M. T. Spahn[1‡]

Throughout the four phases of protein biosynthesis—initiation, elongation, termination, and recycling—the ribosome is controlled and regulated by at least one specified translational guanosine triphosphatase (trGTPase). Although the structural basis for trGTPase interaction with the ribosome has been solved for the last three steps of translation, the high-resolution structure for the key initiation trGTPase, initiation factor 2 (IF2), complexed with the ribosome, remains elusive. We determine the structure of IF2 complexed with a nonhydrolyzable guanosine triphosphate analog and initiator fMet-tRNA$_i^{Met}$ in the context of the *Escherichia coli* ribosome to 3.7-Å resolution using cryo-electron microscopy. The structural analysis reveals previously unseen intrinsic conformational modes of the 70*S* initiation complex, establishing the mutual interplay of IF2 and initator transfer RNA (tRNA) with the ribsosome and providing the structural foundation for a mechanistic understanding of the final steps of translation initiation.

INTRODUCTION

Initiation of translation is an intensively regulated multistep reaction (*1*). In bacteria, binding of initiator fMet-tRNA$_i^{Met}$ to the AUG start codon at the P-site of the 30*S* subunit defines the correct reading frame of the mRNA. Formation of the 30*S* initiation complex (30*S*-IC) is aided by three universal initiation factors (IFs): IF1, IF2 and IF3. The translational guanosine triphosphatase (GTPase) IF2, a key player of the late steps of the initiation reaction (*2*), facilitates the association of the 30*S*-IC with the large 50*S* ribosomal subunit to form the 70*S*-IC. IF2 is composed of five domains, including a less conserved N-terminal domain followed by the C-terminal domains I to IV (*3*). Domain I confers GTPase activity and, together with domains II and III, the ability to bind directly to the 30*S* subunit (*4*), whereas the C-terminal domain IV promotes interaction with the initiator fMet-tRNA$_i^{Met}$ (*5*, *6*). A recent x-ray study of IF2 revealed the structure of all the domains except domain IV (*4*, *7*), and low-resolution cryo-electron microscopy (cryo-EM) maps depict the overall location of IF2 between the ribosomal subunits (*8*–*11*). However, high-resolution structural information on ribosome-bound IF2 and its interactions with ribosome and initiator transfer RNA (tRNA) remain elusive, precluding a mechanistic understanding of the functional role of IF2.

RESULTS

To solve the structure of ribosome-bound IF2, the factor was stalled on programmed 70*S* ribosomes by the nonhydrolyzable GTP analog guanylylimidodiphosphate (GDPNP) in the presence of fMet-tRNA$_i^{Met}$. Although previous cryo-EM analysis depicted only one major state (*4*, *8*), multiparticle refinement (*12*) of our cryo-EM data resulted in two cryo-EM maps for subpopulations of the 70*S*–fMet-tRNA$_i^{Met}$–IF2–GDPNP complex (Fig. 1 and fig. S1). These differ significantly in the rotational state of the ribosomal subunits, the position of the L1 stalk, and the binding mode of the fMet-tRNA$_i^{Met}$. The smaller subpopulation (70*S*-IC I; 14,874 particle images, 4.6-Å resolution) is in a fully rotated ribosome state, with the 30*S* rotated by 8.4° and the 30*S* head mildly swiveled by 2.4° compared to the classical 70*S* ribosome conformation (*13*) (Fig. 1C). The larger subpopulation (70*S*-IC II; 54,585 particle images, 3.7-Å resolution) is in a semirotated state and undergoes only a moderate intersubunit rotation of 3.7° (Fig. 1F). The near-atomic resolution of major parts of the reconstruction of the 70*S*-IC II (Fig. 1, G to I, and fig. S2) facilitated atomic model building, aided by existing crystal structures. Although the overall structure is in general agreement with previous cryo-EM analysis (*4*, *8*), there are several pronounced differences. For example, the C-terminal domain IV of IF2 is rotated by ~180°, compared to previous cryo-EM models (*4*, *8*) in our present structure (fig. S3).

Ribosomal intersubunit rotation affects the binding states of initiator fMet-tRNA$_i^{Met}$ (Fig. 2). Although in both substates the AUG start codon and fMet-tRNA$_i^{Met}$ anticodon stem loop stay bound in the P-site of the 30*S* subunit (Fig. 2A), the tRNAs are differentially positioned relative to the 50*S* subunit (Fig. 2B). The codon-anticodon duplex within the 70*S*-IC I is similar in position to a canonical P/E tRNA (*13*), and the elbow of the fMet-tRNA$_i^{Met}$ also interacts with the L1 stalk (fig. S4). At first glance, this position of the fMet-tRNA$_i^{Met}$ elbow is surprising because the 50*S* E-site is specific for deacylated tRNA (*14*, *15*). However, the tRNA adopts a unique conformation and binding mode because the acceptor stem is bent toward the P-site and the 3′-CCA–fMet end is displaced by more than 20 Å to interact with IF2 domain IV (Fig. 2B). We term this novel chimeric tRNA state of the 70*S*-IC I complex the P/ei state (30*S* P-site, 50*S* E-site, and IF2). In the 70*S*-IC II complex, the initator tRNA is located closer to the P-site (Fig. 2B), and the tRNA elbow interacts with the central protuberance (CP) of the 50*S* subunit. Accordingly, we term this the P/pi state. Overall, the position of the P/pi-tRNA is similar but not identical to the P/I-tRNA previously delineated at lower resolution (*8*). Because the interaction with the L1 stalk, which has been previously reported for the P/I-tRNA, is only observed for the P/ei-tRNA but not for the P/pi-tRNA, we may have disentangled a previously inseparable P/I-tRNA into P/pi and P/ei-states (fig. S4).

[1]Institut für Medizinische Physik und Biophysik, Charité–Universitätsmedizin Berlin, Charitéplatz 1, 10117 Berlin, Germany. [2]UltraStrukturNetzwerk, Max Planck Institute for Molecular Genetics, Ihnestrasse 73, 14195 Berlin, Germany.
*Present address: Institut für Medizinische Physik und Biophysik, AG ProteInformatics, Charité–Universitätsmedizin Berlin, Charitéplatz 1, 10117 Berlin, Germany.
†Present address: Institut für Medizinische Physik und Biophysik, AG Protein X-ray Crystallography and Signal Transduction, Charité–Universitätsmedizin Berlin, Charitéplatz 1, 10117 Berlin, Germany.
‡Corresponding author. E-mail: christian.spahn@charite.de

Downloaded from http://advances.sciencemag.org/ on April 11, 2017

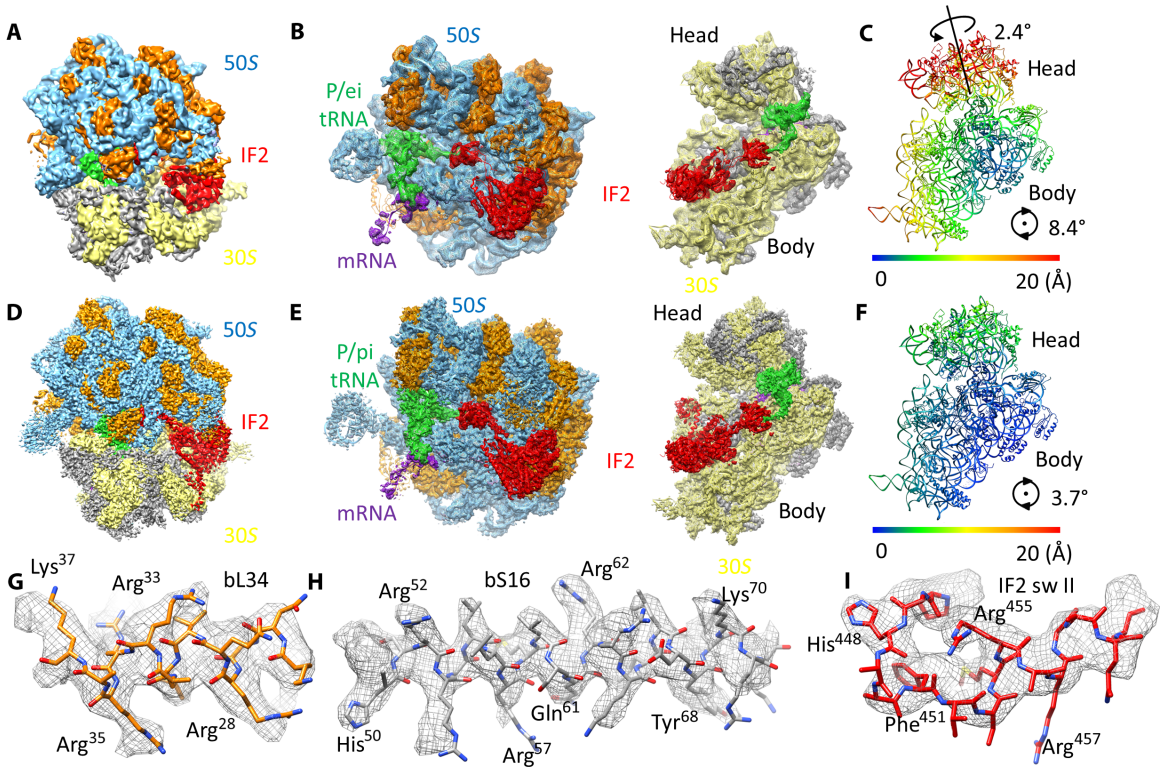

Fig. 1. Overview of the cryo-EM reconstruction of the two distinct 70*S* initiation complexes. (**A** to **F**) Overview of the cryo-EM reconstruction of the 70*S*-IC I complex (A to C) and of the 70*S*-IC II complex (D to F). The cryo-EM maps (blue, 23*S* and 5*S* rRNA; orange, L proteins; yellow, 16*S* rRNA; gray, S proteins; green, fMet-tRNA$_i^{Met}$; red, IF2) (A and D) and mesh representation of the cryo-EM maps separated into ribosomal subunits with docked models (blue, 23*S* and 5*S* rRNA; orange, L proteins; yellow, 16*S* rRNA; gray, S proteins; green, fMet-tRNA$_i^{Met}$; red, IF2; purple, mRNA) (B and E) are shown. (C and F) View from the intersubunit space onto the models of 30*S* subunit depicted as ribbons. Elements are colored according to their structural displacement compared to the classical (*13*) conformation upon 50*S* alignment. The directions and magnitudes of the intersubunit rotation and head swivel for the 70*S*-IC I complex (C) and the 70*S*-IC II complex (F) are indicated. (**G** to **I**) Enlarged regions of the cryo-EM map of the 70*S*-IC II at 3.7-Å resolution, showing bL34 (G), bS16 (H), and IF2 (I) (gray, cryo-EM density; orange, bL34; gray, bS16; red, IF2).

Relative to the 30*S*, the fMet-tRNA$_i^{Met}$ appears to follow the 30*S* head swivel, resulting in a small tilting toward the E-site for the P/ei-tRNA compared to the P/pi-tRNA (Fig. 2A). A similar observation has been made by Julián and colleagues (*11*) based on a lower-resolution cryo-EM map of a 30*S*-IC containing fMet-tRNA$_i^{Met}$ and all three initiation factors. The striking resemblance between the 30*S*-IC and the equivalent parts of the fully rotated 70*S*-IC I substate suggests that this state is close to the state immediately after subunit joining. The semirotated 70*S*-IC II substate in turn resembles an intermediate state on the way to the nonrotated classical elongation state. This assignment is in overall agreement with single-molecule fluorescence resonance energy transfer data reporting an early 70*S*-IC in the rotated state that is converted into an elongation-competent 70*S* complex by back rotation of the 30*S* subunit (*16*, *17*). The fact that we have not detected a nonrotated ribosome state can be explained by the fact that the full back rotation requires GTP hydrolysis by IF2.

Going from the 70*S*-IC I to the 70*S*-IC II, both the body of the fMet-tRNA$_i^{Met}$ and the core domains of IF2 essentially follow the partial back rotation of the 30*S* subunit (Fig. 3A). In contrast, domain IV of IF2 is hardly moving, keeping its location in the neighborhood of the 50*S* peptidyl transferase center and interactions with ribosomal protein uL16 and 23*S* rRNA helices H89 and H71. Domain IV of IF2 in turn retains the 3′-A-fMet of the initiator tRNA, which is cradled by the two apical β1-β2 and β4-β5 loops (Fig. 3B). The IF2 domain IV/A76-fMet module is linked by flexible regions to the core of IF2 and the body of the tRNA, respectively, to uncouple the motion and to buffer the rotational movement of the 30*S* subunit. On the IF2 side, a flexible loop connects domain IV that extends from helix 12 of domain III. This is different to the homologous eukaryotic eIF5B, where a more rigid α helix links domain IV to the core of eIF5B, and where both elements together follow the 40*S* subunit rolling (*18*) (fig. S5). On the tRNA side, the 3′-CCA end is differently kinked in both states and appears to be dynamic. A defining feature of initiator tRNA is the absence of the first base pair in the acceptor stem. This may support the structural dynamics within the 70*S*-IC by increasing the length of the single-stranded 3′ end. Thus, the present finding suggests a role for the tRNA$_i^{Met}$ C1:A72 mismatch besides its functional role during formylation (*19*, *20*).

Although there may be still some ambiguity in the exact details, the single-residue resolution of the 70*S*-IC II cryo-EM map provides insight into the contact between the IF2 domain IV and the CCA-fMet end of the tRNA (fig. S6). The terminal fMet-A76 is bound in a pocket formed by Ser^{844}, Arg^{846}, Arg^{847}, Phe^{848}, and Lys^{849} from the β4-β5 loop; Phe^{804}, Phe^{809}, Ile^{812}, and Cys^{815} from the β1-β2 loop; and Glu^{860}, Cys^{861}, and Gly^{862} from β5 (Fig. 3B). The interaction of A76 with IF2 domain IV seems to resemble closely the interaction of the homologous elongation factor Tu (EF-Tu) domain II with elongator

Downloaded from http://advances.sciencemag.org/ on April 11, 2017

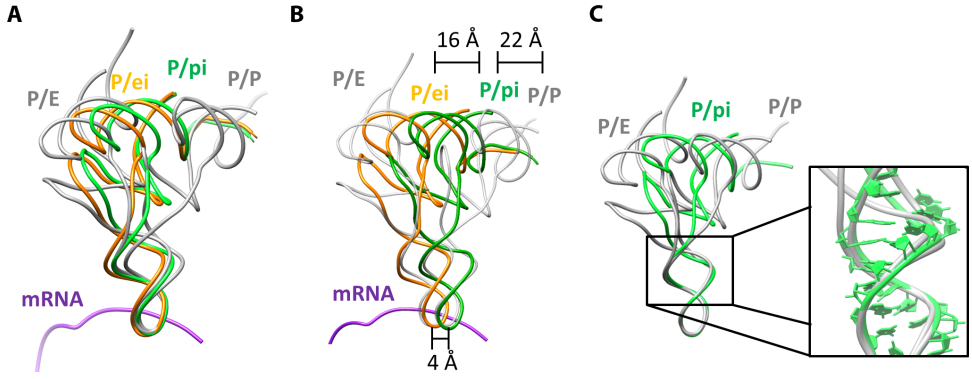

Fig. 2. Binding state of the fMet-tRNA^{fMet}. (**A** and **B**) Comparison of the position of P/pi-tRNA (green) and P/ei-tRNA (orange) with classical P-site and hybrid P/E-site (gray) (*13*) [Protein Data Bank (PDB) ID 4V9D] tRNAs upon 30*S* (A) and 50*S* alignment (B). Compared to the P/P tRNA, the elbow of the P/pi tRNA is shifted by 22 Å toward the E-site, and the codon-anticodon duplex of the P/ei-tRNA is shifted by 4 Å toward the E-site. Compared to the P/pi tRNA, the elbow of the P/ei-tRNA is displaced by additional 16 Å toward the E-site to allow interaction with the oncoming L1 stalk. (**C**) Conformation of the P/pi tRNA (green) compared to the P/E and P/P (gray) conformations upon anticodon stem loop (ASL) alignment; highlighted is the hinge region of the tRNAs.

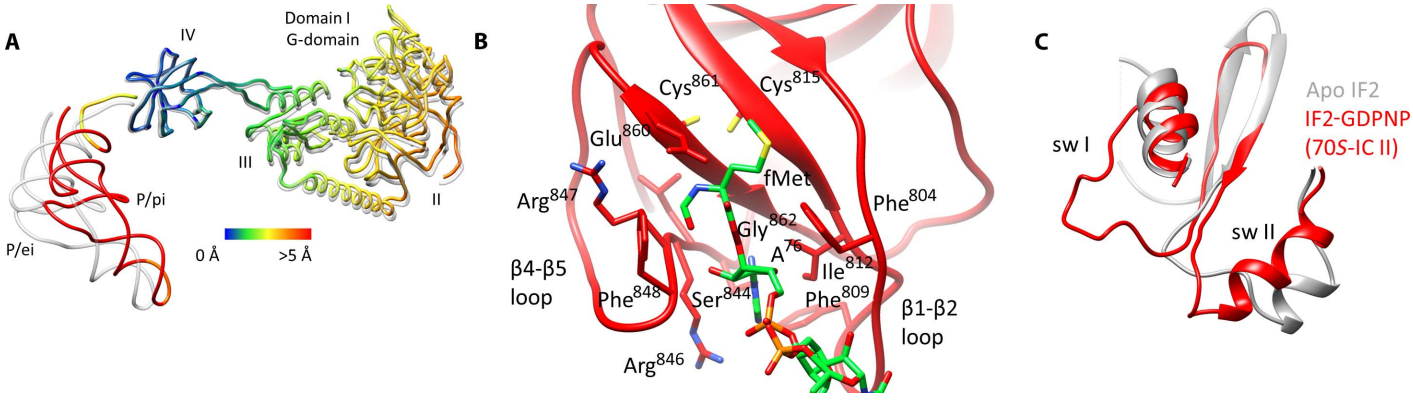

Fig. 3. IF2 on the ribosome. (**A**) Superposition of IF2 and initiator tRNA in 70*S*-IC I (gray) and 70*S*-IC II complexes upon 50*S* alignment. The distances between both substates are color-coded (capped at 5 Å). (**B**) Model for the interaction of the 3′-CCA of the fMet-tRNA$_i^{Met}$ (green) with domain IV of IF2 (red). Important residues for the binding interaction are indicated. (**C**) Comparison of the switch regions in *Thermus thermophilus* apo IF2 (*7*) (PDB ID 4KJZ, chain B) (gray) and *Escherichia coli* IF2-GDPNP (red) upon G-domain alignment.

tRNAs; the fMet is cradled by Arg^{847} and Phe^{848} and seems to be positioned by backbone interactions between the formyl group and the Nα of Phe^{848}. These binding site interactions are in agreement with biochemical and nuclear magnetic resonance spectroscopic data (*21*) and rationalize why the introduction of a partially negative charge from the formyl group leads to a 170-fold increased rate of initiation (*22*). Our model also explains the role of Cys^{861} and Cys^{815} that presumably stabilize the backbone geometry of the binding pocket through a disulfide bond (*23*), and further rationalizes that mutations of Gly^{862} to larger amino acids substantially reduce the binding affinity of IF2 to fMet-tRNA^{fMet} (*21*) because this would lead to a clash with the ligand (fig. S6).

In both 70*S*-IC complexes, the IF2 core domains I to III are bound in the classical factor binding site (Fig. 1) in an overall similar configuration to EF-G and EF-Tu (*24*). Switch I (sw I) and sw II are well defined and found in a different configuration compared to recent x-ray structures of the isolated IF2 (*7*) (Fig. 3C). The sarcin-ricin loop [SRL; helix 95 of 23*S* rRNA] of the 50*S* subunit is bound at the interface between domains I and III. The universally conserved Tyr^{772} within IF2 helix 12 of domain III is in close proximity to the SRL, similar to the eukaryotic system (*18*, *25*). Remarkably, the partial back rotation of the 30*S* subunit brings the G-domain of IF2, in particular His^{448} of the sw II loop, closer to the SRL when transitioning from the 70*S*-IC I to the 70*S*-IC II. A contact between His^{448} (His^{84} in EF-Tu) of the sw II loop and the SRL has been deemed important for GTP hydrolysis of EF-G (*26*–*28*) (fig. S7). Therefore, GTP hydrolysis may be regulated by the back rotation of the 30*S* subunit.

Our results indicate how IF2, by modulating the state of fMet-tRNA$_i^{Met}$ and by exploiting spontaneous intersubunit rotation of the ribosome, facilitates joining of the large subunit and the subsequent transition into an elongation-competent 70*S* complex (Fig. 4). As proposed (*10*), fMet-tRNA$_i^{Met}$ and IF2 aid subunit joining by creating a large scaffold at the subunit interface and providing contact regions with the 50*S* subunit. However, similar to the eukaryotic system (*18*), a major problem during initiation is not subunit joining per se but subunit joining with the 30*S*-IC, where initiator tRNA is already bound to the P-site of the small ribosomal subunit. The space between helix 69 of the 23*S* rRNA and uL5 of the CP of the 50*S* subunit is too narrow for the tRNA to pass through in its canonical conformation (fig. S8). Our results suggest how this problem is solved during bacterial initiation. Aided by IF2, the initiator tRNA is first bound to the 50*S* E-site region in the fully rotated 70*S*-IC I. Back rotation of the 30*S*

Downloaded from http://advances.sciencemag.org/ on April 11, 2017

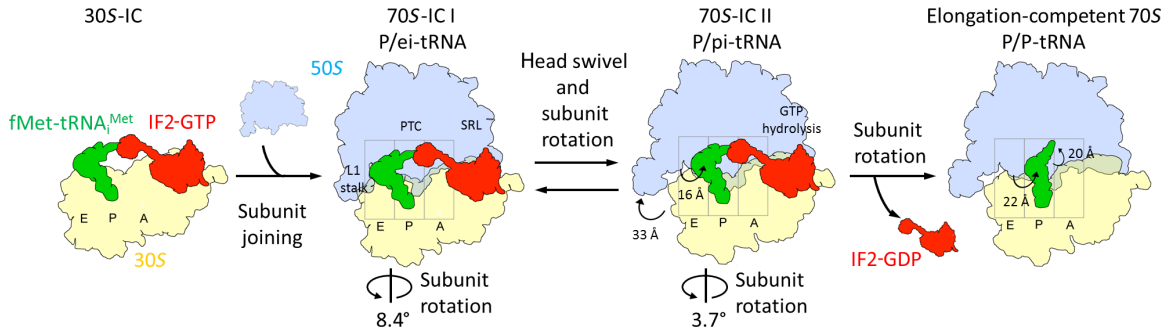

Fig. 4. Scheme of the late steps of initiation. IF2 (red)–induced subunit joining of the 30*S* IC (yellow) with the 50*S* (blue) subunit occurs in a rotated conformation and leads to the formation of the 70*S*-IC I. The initiator tRNA (green) is positioned in the P/ei state through interactions with the L1 stalk and domain IV of IF2. Partial back rotation and unswiveling facilitate the P/pi state of initiator tRNA and reorient the G-domain of IF2 to trigger GTP hydrolysis. To reach the elongation-competent 70*S* complex, the 30*S* subunit completes back rotation, IF2-GDP dissociates, and the initiator tRNA completes the partial reverse translocation on the 50*S* subunit to reach the P/P-site state. Movements of elbow and acceptor stem are indicated.

subunit then facilitates a partial reverse translocation of initiator tRNA relative to the 50*S* subunit (Fig. 4). A comparison to our mammalian initiation complex (*18*) shows that the late steps of initiation uses large-scale conformational changes of the ribosome in both domains of life. Nevertheless, there are striking differences in the molecular strategy to load initiator tRNA. Whereas the eukaryotic initiation uses eukaryotic-specific subunit rolling (*18*, *29*), the bacterial IF2-dependent initiation uses subunit rotation. The unique P/ei and P/pi states of the tRNA require the tRNA to adopt a specific conformation to simultaneously undergo codon-anticodon interaction and interactions with domain IV of IF2. Specific features of the initiator tRNA appear to facilitate these particular intermediate states. Thus, the P/ei and P/pi states presumably resemble checkpoints to ensure binding of the correct tRNA. In this sense, the complex pathway of IF2-promoted subunit joining may not only ensure efficient loading of the fMet-tRNA^{fMet} into the 50*S* P-site but may also be used to provide discriminative power for accurate selection of initiator over elongator tRNAs.

MATERIALS AND METHODS

Methods

Formation of the 70*S*–fMet-tRNA$_i^{Met}$–IF2–GDPNP complex. His-tagged IF2 from *E. coli* was produced using the T5 expression system. Recombinant IF2 was isolated by affinity chromatography and ion-exchange chromatography. The mRNA with the sequence 5′-GGGCAAAACAAAAGGAGGCUAAAU**AUG**UUCUAGCAAAACA-AAACAAAAGAAUU-3′ was transcribed using the T7-MEGAshortscript (Ambion). The mRNA contains a strong Shine-Dalgarno sequence (underlined) and the initiator AUG start codon (bold). The fMet-tRNA$_i^{Met}$ was made from tRNA$_i^{Met}$ (Sigma). The tRNA was aminoacylated and N-formylated as described previously (*30*) and purified via Nucleosil C_4 column (Macherey-Nagel). Tightly coupled 70*S* ribosomes from the *E. coli* CAN20 strain were purified as described (*31*). The fMet-tRNA$_i^{Met}$–IF2–GDPNP complex was formed by incubating 24-pmol ribosomes with 400-pmol mRNA, 100-pmol tRNA, and 115-pmol IF2 in the presence of 50 nmol of the nonhydrolyzable GTP analog GDPNP at 37°C for 15 min in Buffer B15 [20 mM Hepes-KOH (pH 7.5), 15 mM magnesium acetate, 150 mM potassium acetate, 4 mM β-mercapthoethanol, 2 mM spermidine, and 0.05 mM spermine]. The occupancy of IF2 in the complex was about 40 to 50%, as determined by Western blotting against the 6×His-tag of IF2 and the uL1 protein following a sucrose density centrifugation.

Cryo-EM and image processing. Ribosomal complexes were diluted to a concentration of 30 nM and flash-frozen in liquid ethane on glow-discharged carbon-coated grids (Quantifoil Micro Tools GmbH) using a Vitrobot device (FEI). In total, two sets of images were collected under low-dose conditions (20 $e^{-}Å^{-2}$) on a Tecnai G^2 Polara Microscope (FEI) operating at 300 kV and equipped with a K2 Summit detector (Gatan) at ×31,000 nominal magnification in SuperResolution mode resulting in a pixel size of 0.615 Å per pixel. Data were collected automatically using Leginon (*32*) at a defocus range of 0.5 to 5 μm.

The initial contrast transfer function defocus values for the micrographs were estimated from the contrast transfer function using CTFfind4 (*33*). Ribosomal projection images were (semi)automatically identified with SIGNATURE (*34*) and e2boxer from the EMAN2 software package (*35*). In total, 232,659 particle images were selected from 3715 micrographs. The data set was individually aligned by using a low-resolution 70*S* from *E. coli* as reference using the multiparticle refinement (*12*) in SPIDER (*36*). After initial refinement, bad particle images were removed. During unsupervised classification, the data set split into structures showing IF2 bound to ribosomes in two different conformations. These two conformations were isolated from each other and refined separately. Particle images that did not contain the two large ligands IF2 and fMet-tRNA$_i^{Met}$ were selected out and not considered for further analysis. After interpolation to a pixel size of 1.23 Å per pixel, a total number of 14,874 particle images corresponding to the fully rotated conformation were refined using SPIDER (*36*) and SPARX (*37*). A total number of 54,585 particle images corresponding to an intermediate rotated conformation were interpolated to a pixel size of 1.025 Å per pixel and refined using SPIDER (*36*) and SPARX (*37*).

Structural models. Existing atomic models of the *E.coli* ribosome were adjusted to the derived densities. Initial rigid body docking of x-ray structures of the ribosomal 50*S* subunit [PDB ID 4V9O for subpopulation II and 3R8S for subpopulation I (*13*)], 30*S* head, and 30*S* body [4GD1 for subpopulation I, 4GD2 for subpopulation II (*13*)] was performed using UCSF Chimera (*38*). Flexible elements of the docked models were subsequently adjusted to the derived densities in COOT (*39*). The near-atomic resolution of substate II enabled us to build a model for IF2 in COOT (*39*) based on a homology model composed of the core region of the solution structure of *T. thermophilus* IF2 (*7*) and the C-terminal domain IV from *Bacillus stearothermophilus*

Downloaded from http://advances.sciencemag.org/ on April 11, 2017

(*40*). Subsequently, the model was globally idealized using REFMAC (*41*) and validated with MolProbity (*42*). For the AUG start codon and fMet-tRNA^{fMet} (PDB 5AFI), two rigid units comprising either the ASL and AUG start codon or the acceptor arm, together with the tRNA elbow (TΨ- and D-loop), were combined by allowing flexibility around ASL–tRNA elbow junction, a flexible hinge region that was already observed when tRNAs adopt hybrid A/T or P/E tRNA binding states (*13*, *43*–*45*). The single-stranded CCA end was built manually into the derived density in COOT (*39*), and the initial fitting was globally idealized using ERRASER (*46*). The structure of poorly resolved, flexible loops in IF2 was predicted by FragFit, a fragment-based tool for modeling of missing protein segments into cryo-EM density maps (see section below). These initial models were then refined by real-space refinement in Phenix 1.10. To prevent overfitting of the weight of the map versus model, geometry was estimated using cryo-EM maps from half-sets as introduced for reciprocal space refinement (*47*, *48*) (fig. S2B). The derived models of IF2 and the mRNA tRNA module from subpopulation II were subsequently docked as rigid bodies into the map of subpopulation I.

Validation with FragFit. The FragFit database (http://proteinformatics.charite.de/fragfit) is constructed from about 90,000 protein structures, deposited in PDB (as of June 2013). Extraction of all overlapping peptide fragments with lengths between 3 and 35 amino acids yielded more than 700 million fragments. For each fragment, the sequence, PDB identifier, and a geometrical fingerprint of the stem atoms are stored in the database. This fingerprint is composed of the distance between the stem atoms and three angles depicting the relative orientation of the stem amino acids to each other. The program searches for matches between a missing fragment in the protein structure and fragments of the same length, with similar sequence and similar geometrical fingerprint stored in the database.

The search process follows a stepwise approach to minimize the search time. (i) In the first step, fragments of a specified length with a root mean square deviation of the terminal atoms to the stem atoms of the gap of less than 0.75 Å are selected. (ii) In the second step, the 500 candidates with best fit are selected. These 500 candidates are re-ranked on the basis of their sequence similarity to the missing fragment and the geometrical fingerprint. (iii) In a third step, FragFit uses cryo-EM density maps to calculate a cross-correlation to the artificial density derived from the identified fragments. The cross-correlation, which is used to rescore the fragments obtained during steps (i) and (ii), is calculated with the SPIDER software package (*36*). To minimize the computational load and to speed up the cross-correlation search, the box size is reduced to the definite section of the cryo-EM map. For that purpose, a box is estimated from the length of the missing fragment and the distance between the stem atoms and the cut from the cryo-EM map. To exclude false positives, densities already occupied by atoms are deleted from the map. The fragments with the highest Pearson cross-correlation coefficient between artificial and experimentally determined density map are selected for visual inspection.

SUPPLEMENTARY MATERIALS

Supplementary material for this article is available at http://advances.sciencemag.org/cgi/content/full/2/3/e1501502/DC1

Materials and Methods

Fig. S1. Overview of three-dimensional classification.

Fig. S2. Resolution estimations of the 70S-IC complexes.

Fig. S3. Comparison of the present *E. coli* IF2 with previous models.

Fig. S4. Comparison of the tRNA positions.

Fig. S5. Comparison of the present ribosome-bound IF2 with ribosome-bound EF-Tu, ribosome-bound eIF5b, and the x-ray structure of IF2.

Fig. S6. Comparison of the tRNA binding domains II of EF-Tu and IV of IF2.

Fig. S7. Back rotation of the 30*S* subunits positions the G-domain of IF2 onto the SRL.

Fig. S8. Subunit joining requires repositioning of the initiator tRNA.

Table S1. Model statistics.

Reference (*49*)

REFERENCES AND NOTES

1. A. Marintchev, G. Wagner, Translation initiation: Structures, mechanisms and evolution. *Q. Rev. Biophys.* **37**, 197–284 (2004).
2. A. Simonetti, S. Marzi, L. Jenner, A. Myasnikov, P. Romby, G. Yusupova, B. P. Klaholz, M. Yusupov, A structural view of translation initiation in bacteria. *Cell. Mol. Life Sci.* **66**, 423–436 (2009).
3. C. O. Gualerzi, L. Brandi, E. Caserta, C. Garofalo, M. Lammi, A. La Teana, D. Petrelli, R. Spurio, J. Tomsic, C. L. Pon, Initiation factors in the early events of mRNA translation in bacteria. *Cold Spring Harb. Symp. Quant. Biol.* **66**, 363–376 (2001).
4. A. Simonetti, S. Marzi, I. M. L. Billas, A. Tsai, A. Fabbretti, A. G. Myasnikov, P. Roblin, A. C. Vaiana, I. Hazemann, D. Eiler, T. A. Steitz, J. D. Puglisi, C. O. Gualerzi, B. P. Klaholz, Involvement of protein IF2 N domain in ribosomal subunit joining revealed from architecture and function of the full-length initiation factor. *Proc. Natl. Acad. Sci. U.S.A.* **110**, 15656–15661 (2013).
5. B. S. Laursen, H. P. Sørensen, K. K. Mortensen, H. U. Sperling-Petersen, Initiation of protein synthesis in bacteria. *Microbiol. Mol. Biol. Rev.* **69**, 101–123 (2005).
6. R. Spurio, L. Brandi, E. Caserta, C. L. Pon, C. O. Gualerzi, R. Misselwitz, C. Krafft, K. Welfle, H. Welfle, The C-terminal subdomain (IF2 C-2) contains the entire fMet-tRNA binding site of initiation factor IF2. *J. Biol. Chem.* **275**, 2447–2454 (2000).
7. D. Eiler, J. Lin, A. Simonetti, B. P. Klaholz, T. A. Steitz, Initiation factor 2 crystal structure reveals a different domain organization from eukaryotic initiation factor 5B and mechanism among translational GTPases. *Proc. Natl. Acad. Sci. U.S.A.* **110**, 15662–15667 (2013).
8. G. S. Allen, A. Zavialov, R. Gursky, M. Ehrenberg, J. Frank, The cryo-EM structure of a translation initiation complex from *Escherichia coli*. *Cell* **121**, 703–712 (2005).
9. A. G. Myasnikov, S. Marzi, A. Simonetti, A. M. Giuliodori, C. O. Gualerzi, G. Yusupova, M. Yusupov, B. P. Klaholz, Conformational transition of initiation factor 2 from the GTP- to GDP-bound state visualized on the ribosome. *Nat. Struct. Mol. Biol.* **12**, 1145–1149 (2005).
10. A. Simonetti, S. Marzi, A. Myasnikov, A. Fabbretti, M. Yusupov, C. O. Gualerzi, B. P. Klaholz, Structure of the 30S translation initiation complex. *Nature* **455**, 416–420 (2008).
11. P. Julián, P. Milon, X. Agirrezabala, G. Lasso, D. Gil, M. V. Rodnina, M. Valle, The Cryo-EM structure of a complete 30S translation initiation complex from Escherichia coli. *PLOS Biol.* **9**, e1001095 (2011).
12. J. Loerke, J. Giesebrecht, C. M. T. Spahn, Multiparticle cryo-EM of ribosomes. *Methods Enzymol.* **483**, 161–177 (2010).
13. J. A. Dunkle, L. Wang, M. B. Feldman, A. Pulk, V. B. Chen, G. J. Kapral, J. Noeske, J. S. Richardson, S. C. Blanchard, J. H. D. Cate, Structures of the bacterial ribosome in classical and hybrid states of tRNA Binding. *Science* **332**, 981–984 (2011).
14. R. Lill, A. Lepier, F. Schwägele, M. Sprinzl, H. Vogt, W. Wintermeyer, Specific recognition of the 3′-terminal adenosine of tRNA^{Phe} in the exit site of *Escherichia coli* ribosomes. *J. Mol. Biol.* **203**, 699–705 (1988).
15. T. M. Schmeing, P. B. Moore, T. A. Steitz, Structures of deacylated tRNA mimics bound to the E site of the large ribosomal subunit. *RNA* **9**, 1345–1352 (2003).
16. R. A. Marshall, C. E. Aitken, J. D. Puglisi, GTP hydrolysis by IF2 guides progression of the ribosome into elongation. *Mol. Cell* **2**, 37–47 (2009).
17. A. Tsai, A. Petrov, R. A. Marshall, J. Korlach, S. Uemura, J. D. Puglisi, Heterogeneous pathways and timing of factor departure during translation initiation. *Nature* **487**, 390–393 (2012).
18. H. Yamamoto, A. Unbehaun, J. Loerke, E. Behrmann, M. Collier, J. Bürger, T. Mielke, C. M. T. Spahn, Structure of the mammalian 80S initiation complex with initiation factor 5B on HCV-IRES RNA. *Nat. Struct. Mol. Biol.* **21**, 721–727 (2014).
19. C. Mayer, U. RajBhandary, Conformational change of *Escherichia coli* initiator methionyl-tRNA^{fMet} upon binding to methionyl-tRNA formyl transferase. *Nucleic Acids Res.* **30**, 2844–2850 (2002).
20. E. Schmitt, M. Panvert, S. Blanquet, Y. Mechulam, Crystal structure of methionyl-tRNA$_f^{Met}$ transformylase complexed with the initiator formyl-methionyl-tRNA$_f^{Met}$. *EMBO J.* **17**, 6819–6826 (1998).
21. M. Guenneugues, E. Caserta, L. Brandi, R. Spurio, S. Meunier, C. L. Pon, R. Boelens, C. O. Gualerzi, Mapping the fMet-tRNA$_f^{Met}$ binding site of initiation factor IF2. *EMBO J.* **19**, 5233–5240 (2000).

Downloaded from http://advances.sciencemag.org/ on April 11, 2017

22. A. Antoun, M. Y. Pavlov, M. Lovmar, M. Ehrenberg, How initiation factors tune the rate of initiation of protein synthesis in bacteria. *EMBO J.* **25**, 2539–2550 (2006).
23. R. Misselwitz, K. Welfle, C. Krafft, H. Welfle, L. Brandi, E. Caserta, C. O. Gualerzi, The fMet-tRNA binding domain of translational initiation factor IF2: Role and environment of its two Cys residues. *FEBS Lett.* **459**, 332–336 (1999).
24. R. M. Voorhees, V. Ramakrishnan, Structural basis of the translational elongation cycle. *Annu. Rev. Biochem.* **82**, 203–236 (2013).
25. I. S. Fernández, X.-C. Bai, T. Hussain, A. C. Kelley, J. R. Lorsch, V. Ramakrishnan, S. H. W. Scheres, Molecular architecture of a eukaryotic translational initiation complex. *Science* **342**, 1240585 (2013).
26. Y. Chen, S. Feng, V. Kumar, R. Ero, Y.-G. Gao, Structure of EF-G–ribosome complex in a pretranslocation state. *Nat. Struct. Mol. Biol.* **20**, 1077–1084 (2013).
27. D. S. Tourigny, I. S. Fernández, A. C. Kelley, V. Ramakrishnan, Elongation factor G bound to the ribosome in an intermediate state of translocation. *Science* **340**, 1235490 (2013).
28. A. Pulk, J. H. D. Cate, Control of ribosomal subunit rotation by elongation factor G. *Science* **340**, 1235970 (2013).
29. T. V. Budkevich, J. Giesebrecht, E. Behrmann, J. Loerke, D. J. F. Ramrath, T. Mielke, J. Ismer, P. W. Hildebrand, C.-S. Tung, K. H. Nierhaus, K. Y. Sanbonmatsu, C. M. T. Spahn, Regulation of the mammalian elongation cycle by subunit rolling: A eukaryotic-specific ribosome rearrangement. *Cell* **158**, 121–131 (2014).
30. R. Jünemann, J. Wadzack, F. J. Triana-Alonso, J.-U. Bittner, J. Caillet, T. Meinnel, K. Vanatalu, K. H. Nierhaus, In vivo deuteration of transfer RNAs: Overexpression and large-scale purification of deuterated specific tRNAs. *Nucleic Acids Res.* **24**, 907–913 (1996).
31. U. A. Bommer, N. Burkhardt, R. Jünemann, C. M. T. Spahn, F. Triana, K. H. Nierhaus, Ribosomes and polysomes, in *Subcellular Fractionation: A Practical Approach*, J. Graham and D. Rickwoods, Eds. (IRL Press, Oxford, 1996), pp. 271–301.
32. C. Suloway, J. Pulokas, D. Fellmann, A. Cheng, F. Guerra, J. Quispe, S. Stagg, C. S. Potter, B. Carragher, Automated molecular microscopy: The new Leginon system. *J. Struct. Biol.* **151**, 41–60 (2005).
33. J. A. Mindell, N. Grigorieff, Accurate determination of local defocus and specimen tilt in electron microscopy. *J. Struct. Biol.* **142**, 334–347 (2003).
34. J. Z. Chen, N. Grigorieff, SIGNATURE: A single-particle selection system for molecular electron microscopy. *J. Struct. Biol.* **157**, 168–173 (2007).
35. G. Tang, L. Peng, P. R. Baldwin, D. S. Mann, W. Jiang, I. Rees, S. J. Ludtke, EMAN2: An extensible image processing suite for electron microscopy. *J. Struct. Biol.* **157**, 38–46 (2007).
36. J. Frank, M. Radermacher, P. Penczek, J. Zhu, Y. Li, M. Ladjadj, A. Leith, SPIDER and WEB: Processing and visualization of images in 3D electron microscopy and related fields. *J. Struct. Biol.* **116**, 190–199 (1996).
37. M. Hohn, G. Tang, G. Goodyear, P. R. Baldwin, Z. Huang, P. A. Penczek, C. Yang, R. M. Glaeser, P. D. Adams, S. J. Ludtke, SPARX, a new environment for Cryo-EM image processing. *J. Struct. Biol.* **157**, 47–55 (2007).
38. E. F. Pettersen, T. D. Goddard, C. C. Huang, G. S. Couch, D. M. Greenblatt, E. C. Meng, T. E. Ferrin, UCSF Chimera—A visualization system for exploratory research and analysis. *J. Comput. Chem.* **25**, 1605–1612 (2004).
39. P. Emsley, K. Cowtan, *Coot*: Model-building tools for molecular graphics. *Acta Crystallogr. D Biol. Crystallogr.* **60**, 2126–2132 (2004).
40. S. Meunier, R. Spurio, M. Czisch, R. Wechselberger, M. Guenneugues, C. O. Gualerzi, R. Boelens, Structure of the fMet-tRNA^{fMet}-binding domain of *B. stearothermophilus* initiation factor IF2. *EMBO J.* **19**, 1918–1926 (2000).
41. G. N. Murshudov, A. A. Vagin, E. J. Dodson, Refinement of macromolecular structures by the maximum-likelihood method. *Acta Crystallogr. D Biol. Crystallogr.* **53**, 240–255 (1997).
42. V. B. Chen, W. B. Arendall III, J. J. Headd, D. A. Keedy, R. M. Immormino, G. J. Kapral, L. W. Murray, J. S. Richardson, D. C. Richardson, *MolProbity*: All-atom structure validation for macromolecular crystallography. *Acta Crystallogr. D Biol. Crystallogr.* **66**, 12–21 (2010).
43. T. M. Schmeing, R. M. Voorhees, A. C. Kelley, Y.-G. Gao, F. V. Murphy IV, J. R. Weir, V. Ramakrishnan, The crystal structure of the ribosome bound to EF-Tu and aminoacyl-tRNA. *Science* **326**, 688–694 (2009).
44. J.-C. Schuette, F. V. Murphy, A. C. Kelley, J. R. Weir, J. Giesebrecht, S. R. Connell, J. Loerke, T. Mielke, W. Zhang, P. A. Penczek, V. Ramakrishnan, C. M. T. Spahn, GTPase activation of elongation factor EF-Tu by the ribosome during decoding. *EMBO J.* **28**, 755–765 (2009).
45. A. H. Ratje, J. Loerke, A. Mikolajka, M. Brünner, P. W. Hildebrand, A. L. Starosta, A. Dönhöfer, S. R. Connell, P. Fucini, T. Mielke, P. C. Whitford, J. N. Onuchic, Y. Yu, K. Y. Sanbonmatsu, R. K. Hartmann, P. A. Penczek, D. N. Wilson, C. M. T. Spahn, Head swivel on the ribosome facilitates translocation by means of intra-subunit tRNA hybrid sites. *Nature* **468**, 713–716 (2010).
46. F.-C. Chou, P. Sripakdeevong, S. M. Dibrov, T. Hermann, R. Das, Correcting pervasive errors in RNA crystallography through enumerative structure prediction. *Nat. Methods* **10**, 74–76 (2013).
47. B. J. Greber, D. Boehringer, M. Leibundgut, P. Bieri, A. Leitner, N. Schmitz, R. Aebersold, N. Ban, The complete structure of the large subunit of the mammalian mitochondrial ribosome. *Nature* **515**, 283–286 (2014).
48. A. Brown, S. Shao, J. Murray, R. S. Hegde, V. Ramakrishnan, Structural basis for stop codon recognition in eukaryotes. *Nature* **524**, 493–496 (2015).
49. A. Kucukelbir, F. J. Sigworth, H. D. Tagare, Quantifying the local resolution of cryo-EM density maps. *Nat. Methods* **11**, 63–65 (2014).

Acknowledgments: We thank T. Hilal, E. Behrmann, A. Schmidt, J. Kalms, and J.T. Christiansen for the helpful discussions. The plasmid for IF2 was provided by K. Nierhaus. We also thank R. Albrecht for the preparation of the reassociated 70*S* ribosomes. We further acknowledge the North-German Supercomputing Alliance (HLRN) for providing computing resources that have contributed to the reported research results. **Funding:** This work was supported by grants from the German Research Foundation (DFG) Forschergruppe 1805 to C.M.T.S.; SFB740 to C.M.T.S., T.M., P.S., and P.W.H.; SFB1078 to P.S.; BI893/8 to P.W.H; and the DFG Cluster of Excellence Unifying Concepts in Catalysis Research Field D3/E3-1 to P.S. **Author contributions:** T.S., D.J.F.R., H.Y., and C.M.T.S. designed the experiments. K.Y. prepared fMet-tRNA$_i^{Met}$. T.S. prepared the 70*S*–fMet-tRNA$_i^{Met}$–IF2–GDPNP complex. J.B and T.M collected cryo-EM data. T.S., J.L., and C.M.T.S. did the image processing. T.S., J.I., P.W.H., and P.S. did the model building. T.S., H.Y., D.J.F.R., and C.M.T.S. discussed the results and wrote the paper. **Competing interests:** The authors declare that they have no competing interests. **Data and materials availability:** The electron density maps and models of the 70*S*-IC complexes have been deposited in the 3D-EM and PDB database with accession numbers EMD-6559 (70*S*-IC II) and EMD-3285 (70*S*-IC I) and PDB IDs 3JCJ (70*S*-IC II) and 3JCN (70*S*-IC I), respectively. All data needed to evaluate the conclusions in the paper are present in the paper and/or the Supplementary Materials. Additional data related to this paper may be requested from the authors.

Submitted 23 October 2015
Accepted 12 January 2016
Published 4 March 2016
10.1126/sciadv.1501502

Citation: T. Sprink, D. J. F. Ramrath, H. Yamamoto, K. Yamamoto, J. Loerke, J. Ismer, P. W. Hildebrand, P. Scheerer, J. Bürger, T. Mielke, C. M. T. Spahn, Structures of ribosome-bound initiation factor 2 reveal the mechanism of subunit association. *Sci. Adv.* **2**, e1501502 (2016).

Downloaded from http://advances.sciencemag.org/ on April 11, 2017

ScienceAdvances
AAAS

Structures of ribosome-bound initiation factor 2 reveal the mechanism of subunit association

Thiemo Sprink, David J. F. Ramrath, Hiroshi Yamamoto, Kaori Yamamoto, Justus Loerke, Jochen Ismer, Peter W. Hildebrand, Patrick Scheerer, Jörg Bürger, Thorsten Mielke and Christian M. T. Spahn (March 4, 2016)

Sci Adv 2016, 2:.
doi: 10.1126/sciadv.1501502

This article is publisher under a Creative Commons license. The specific license under which this article is published is noted on the first page.

For articles published under CC BY licenses, you may freely distribute, adapt, or reuse the article, including for commercial purposes, provided you give proper attribution.

For articles published under CC BY-NC licenses, you may distribute, adapt, or reuse the article for non-commerical purposes. Commercial use requires prior permission from the American Association for the Advancement of Science (AAAS). You may request permission by clicking here.

The following resources related to this article are available online at http://advances.sciencemag.org. (This information is current as of April 11, 2017):

Updated information and services, including high-resolution figures, can be found in the online version of this article at:
http://advances.sciencemag.org/content/2/3/e1501502.full

Supporting Online Material can be found at:
http://advances.sciencemag.org/content/suppl/2016/03/01/2.3.e1501502.DC1

This article **cites 48 articles,** 18 of which you can access for free at:
http://advances.sciencemag.org/content/2/3/e1501502#BIBL

Science Advances (ISSN 2375-2548) publishes new articles weekly. The journal is published by the American Association for the Advancement of Science (AAAS), 1200 New York Avenue NW, Washington, DC 20005. Copyright is held by the Authors unless stated otherwise. AAAS is the exclusive licensee. The title Science Advances is a registered trademark of AAAS

Downloaded from http://advances.sciencemag.org/ on April 11, 2017